Journal of Solid State Chemistry 252 (2017) 119–128

Contents lists available at ScienceDirect

Journal of Solid State Chemistry

journal homepage: www.elsevier.com/locate/jssc

Orbital occupancy evolution across spin- and charge-ordering transitions in $YBaFe_2O_5$

J. Lindén[a], F. Lindroos[a], P. Karen[b,*]

[a] Department of Physics, Åbo Akademi University, FI-20500 Turku, Finland
[b] Department of Chemistry, University of Oslo, P.O.Box 1033 Blindern, N-0315 Oslo, Norway

ARTICLE INFO

Keywords:
Charge ordering
Valence mixing
Planar defects
Mixed valence
Mössbauer spectroscopy
Hyperfine parameters

ABSTRACT

Thermal evolution of the Fe^{2+}–Fe^{3+} valence mixing in $YBaFe_2O_5$ is investigated using Mössbauer spectroscopy. In this high-spin double-cell perovskite, the d^6 and d^5 Fe states differ by the single minority-spin electron which then controls all the spin- and charge-ordering transitions. Orbital occupancies can be extracted from the spectra in terms of the d_{xz}, d_{z^2} and either $d_{x^2-y^2}$ (Main Article) or d_{xy} (Supplement) populations of this electron upon conserving its angular momentum. At low temperatures, the minority-spin electrons fill up the ordered d_{xz} orbitals of Fe^{2+}, in agreement with the considerable orthorhombic distortion of the structure. Heating through the Verwey transition supplies 93% of the mixing entropy, at which point the predominantly mixing electron occupies mainly the $d_{x^2-y^2}/d_{xy}$ orbitals weakly bonding the two Fe atoms that face each other across the bases of their coordination pyramids. This might stabilize a weak coulombic checkerboard order suggested by McQueeney et alii in Phys. Rev. B 87(2013)045127. When the remaining 7% of entropy is supplied at a subsequent transition, the mixing electron couples the two Fe atoms predominantly via their d_{z^2} orbitals. The valence mixing concerns more than 95% of the Fe atoms present in the crystalline solid; the rest is semi-quantitatively interpreted as domain walls and antiphase boundaries formed upon cooling through the Néel and Verwey-transition temperatures, respectively.

1. Introduction

Phase transitions from charge-ordered to valence-mixed states are behind electronic properties such as the colossal magnetoresistance in manganites [1,2] or spin-polarized conduction in magnetite [3–5]. The crystal structure of the charge-ordered magnetite at low temperatures has only recently been solved [6,7], and its complexity extends to the Verwey transition at 120 K [8–10] between the two magnetite forms.

$YBaFe_2O_5$ is a structurally simple model of such Fe^{2+}–Fe^{3+} mixing. Its valence-mixed phase crystallizes as a double-cell perovskite of *Pmmm* symmetry, with Y and Ba atoms ordered into layers [11,12]. The Y layer, free of oxygen atoms, leaves the two $Fe^{2.5+}$ in square-pyramidal coordinations facing each other as a mirror image. These two high-spin iron atoms couple ferromagnetically (FM) in an overall antiferromagnetic (AFM) order of spins along a slightly contracted *b* (as opposed to *a*) of the perovskite cell [11,13]. In the charge-ordered $YBaFe_2O_5$, also these two Fe atoms couple AFM in a magnetic structure of the Wollan–Koehler [14] G-type. The orthorhombic distortion is increased profoundly by ordering the doubly occupied orbitals d_{xz} in the infinite $-Fe^{2+}-O-Fe^{2+}-$ chains along *b* of the *Pmma* structure formed upon further doubling the unit cell [11]. Powder-diffraction methods "see" that the two phases coexist as they convert to each other, and this defines their Verwey-type phase transition as discontinuous.

The d_{xz} orbital ordering was confirmed also by calculations; extended Hückel method was used in Ref. [11] and DFT with the CGA+U approach in Ref. [15]. The latter was applied [16] also for the trickier valence-mixed phase, localizing the valence-mixing electron at the d_{z^2} orbitals of the two Fe atoms, besides a minor $d_{x^2-y^2}$ occupancy.

According to Boltzmann's formula and Stirling approximation, the mixing entropy of two valences is $-2R(\frac{1}{2}\ln\frac{1}{2} + \frac{1}{2}\ln\frac{1}{2}) = 2R\ln 2$ per $YBaFe_2O_5$. Differential scanning calorimetry (DSC) detects about 3/4 of it and reveals that it is acquired in two steps [11,17]. Almost all mixing entropy is supplied at the first step; seen by powder diffraction as a loss of the Fe^{2+}–Fe^{3+} order [11] at the transition temperature denoted T_V. The entropy of the second step, at T_p, is much smaller and no discontinuous structural change is detected by powder diffraction; only a smooth decrease of the tiny orthorhombic distortion that vanishes at the Néel temperature T_N [13,18].

Mössbauer spectroscopy registers a change at all three transitions [19]. When the hyperfine parameters are stripped off their intrinsic

* Corresponding author.
E-mail address: karenp@kjemi.uio.no (P. Karen).

http://dx.doi.org/10.1016/j.jssc.2017.04.036
Received 28 February 2017; Received in revised form 28 April 2017; Accepted 29 April 2017
Available online 01 May 2017
0022-4596/ © 2017 Elsevier Inc. All rights reserved.

temperature dependence, Fe *d*-orbital occupancies can be extracted [20], and a picture emerges of three pairs of mixed-valence iron: charge ordered, intermediate (partially separated) and (nearly) valence mixed, each subsequent pair prevailing at the respective temperature T_V and T_p [21].

Of all its rare-earth variants, $YBaFe_2O_5$ has the highest T_V, transition entropy [17] and valence separation in the charge-ordered state [11]. In this study, the lower oxygen-nonstoichiometry limit of $YBaFe_2O_{5+w}$ is established at various equilibrium conditions, and three such samples of different thermal history are investigated by Mössbauer spectroscopy. The iron-site fraction of the Fe^{2+} minority-spin electron is used to express the transition order parameter in a dedicated program to fit the spectra upon conserving that electron's angular momentum. The obtained Mössbauer parameters are corrected for their intrinsic temperature dependence to reveal changes purely due to the thermally induced valence mixing. Occupancies of *d* orbitals at the two Fe atoms, free of conflicts such as negative values, are obtained between 10 and 415 K, across the two valence-mixing transitions, with a straightforward extrapolation above T_N of the spin-ordering transition. A Mössbauer component previously identified as paramagnetic is assigned to domain walls formed below T_N and anti-phase boundaries below T_V.

2. Materials and methods

Synthesis. The master sample was synthesized from a liquid-mixed citrate precursor [11], calcined and sintered in two batches in flowing gas atmosphere of controlled [22] partial pressure of oxygen at conditions listed in Table 1. The pellets of ~20% porosity were used for quenching [11,22] from high-temperature equilibrium at 1000 °C in flowing atmospheres of O_2 partial pressures set in the interval $-15.66 < \log(p_{O_2}/\text{bar}) < -14.10$ to obtain $YBaFe_2O_{5+w}$ of low nonstoichiometry w or a product reduced to metallic Fe. Since $YBaFe_2O_{5+w}$ is in equilibrium with metallic Fe, the minimum-nonstoichiometry samples were also obtained by annealing with an excess of iron foil (99.5%, Goodfellow, 25 μm) in sealed evacuated silica ampoules at 450 °C. After three months, one of two parallels was quenched in water, the other cooled down at 0.1 °C/min for better equilibration upon the spin- and charge ordering transitions.

Characterization. Oxygen content was determined by cerimetric titration of Fe^{2+} after digestion in 6 M HCl in sealed glass ampoules as described in Ref. [12]. Powder X-ray diffraction patterns were collected with Cu$K_{\alpha 1}$ radiation in a G670 Huber transmission diffractometer up to 100° 2θ and evaluated by Rietveld refinements in the GSAS software suite [23].

DSC. Samples of 90 mg sealed in aluminum pans were scanned in a Perkin–Elmer Pyris 1 calorimeter. Phase-transition thermodynamics was evaluated from scans at 20 K/min between 120 and 350 K calibrated with *n*-dodecane, 3-nitrotoluene, 4-nitrotoluene and a Perkin–Elmer standard indium as detailed in Ref. [17].

Table 1
Calcination and sintering conditions of $YBaFe_2O_5$.

	t (°C)	Ar/H_2	$\log(p_{O_2}/\text{bar})^*$	τ (h)	Color of powder, composition by Rietveld refinement
Calcination batch 1	860	9.43	−18.27	30	black, $YBaFe_2O_{5+w}$
Calcination batch 2	860	53(2)	−16.84(4)	30	red, $YBa_2Fe_3O_8 + YFeO_3$ (=$2YBaFe_2O_5$)
Sintering batch 1	1020	17.9(3)	−17.75(1)	22	black, $YBaFe_2O_{5+w}$
Sintering batch 2	1020	18.8(5)	−17.71(2)	23	black, $YBaFe_2O_{5+w}$

* Standard deviations over the heating period are in brackets. Constant $\log(p_{H_2O}/\text{bar}) = -1.69$.

Transition hysteresis was evaluated by extrapolation to zero scan rate from consecutive cyclic scans between 260 and 360 K at 40, 20, 10 K/min.

Mössbauer spectra and their analysis. Mössbauer spectra were collected on $YBaFe_2O_{5.017}$ quenched from 1000 °C, on $YBaFe_2O_{5.012}$ annealed and quenched, and on $YBaFe_2O_{5.015}$ annealed and slowly cooled. The absorbers were made as described previously [21] and measured in transmission geometry with a Cyclotron Co. ^{57}Co:*Rh* source at fixed temperatures between 11.5 and 450 K and Doppler velocities decreasing from 10.9 mm/s to 2.7 mm/s following the decreasing hyperfine fields. An Oxford CF506 continuous-flow cryostat was used with liquid helium or nitrogen up to 330 K, for higher temperatures a dedicated resistive heater was used operating with nitrogen as a protective atmosphere. Spectral splitting due to AFM below T_N was fitted with the full Hamiltonian of combined electric and magnetic interactions as described previously [19].

The fit parameters were the component intensity I, linewidth Γ constrained equal for all components, internal field B of a Gaussian distribution with a width ΔB (constrained equal for all magnetic sextets), quadrupole-coupling constant eQV_{zz}, asymmetry parameter η fixed to zero for all components except the charge-ordered ones (vide infra), center shift δ, and the angle β between B and eQV_{zz} set to either 0 or 90° due to ambiguity between the angle turning by 90° and sign inversion of V_{zz}.

Specific constraints adopted in the dedicated fit program: Equal intensities for the intermediately ordered pair close to and above T_p, equal intensities for the (nearly) valence-mixed pair of equal separation from $Fe^{2.5+}$, and statistical distribution of Fe valences in each branch of the three mixed-valence pairs (Poisson for charge ordered, Gaussian for intermediate and valence mixed).

3. Calculation and theory

Corrections on intrinsic temperature dependences. The fitted Mössbauer parameters with non-negligible intrinsic temperature dependence, namely center shifts δ and internal fields B, were corrected so that they reveal changes purely due to the thermally induced valence mixing. The δ values decrease with increasing temperature due to a second order Doppler shift caused by thermal vibrations, and this effect is corrected for as described in Ref. [21]. This yields the isomer shift δ_0 and the Debye temperature Θ_D as parameters specific for Fe^{2+}, Fe^{3+} and $Fe^{2.5+}$ (Fig. 1). The internal field B changes due to the thermal decay of the ordered magnetic moment from B^0 at 0 K to zero at T_N. This was modeled as described previously [21] by a mean-field Brillouin-function approximation of $B(T)$ fitted to experimental data along temperature ranges of constant valence, i.e., for the purely charge-

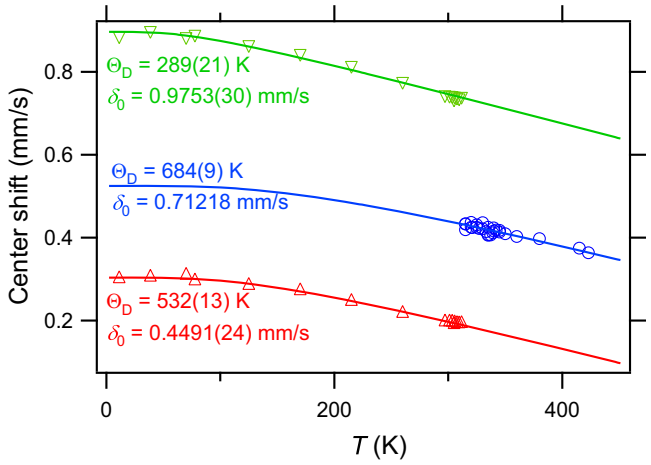

Fig. 1. Least-squares fit of the center shifts δ yielding the isomer shift δ_0 and the Debye temperature Θ_D for Fe^{2+} (▽), Fe^{3+} (△), and $Fe^{2.5+}$ (◯).

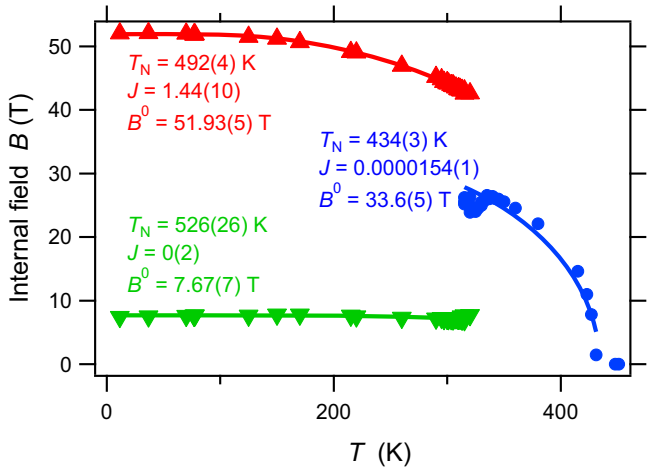

Fig. 2. Least-squares fit that yields parameters B^0, J (total angular momentum quantum number) and T_N for correction of the internal field on thermal decay of ordered magnetic moments (divalent iron component ▼, trivalent ▲, and averaged valence-mixed component •).

ordered and valence-mixed phases. The fit in Fig. 2 yielded parameters from which B^0 was calculated in proportion of either +2 or +3 and +2.5 valences that constitute the component's total valence determined as described in the following paragraph.

Conversion of isomer shift to iron valence. The iron valence of a Mössbauer component at a given temperature point was evaluated by linear interpolation of that point's δ_0 between the standard values shown in Fig. 1. However, the process to calculate δ_0 is based on the value of the valence. The valence and δ_0 are thus not independent of each other and had to be iterated. The valences of each charge-separated pair were then centered around 2.5.

Temperature dependences purely due to valence mixing. The above derived evolutions are purely empirical and were fitted with functions obtained from a sigmoid, $h(T) = h_0 + d/(1 + \exp[(T_{\text{half}} - T)/r])$, by inversion, reversion, shifting or putting on a slope.

Calculations of quadrupole coupling constants. The quadrupole coupling constant eQV_{zz} consists of the nuclear quadrupole moment eQ for the excited ^{57}Fe Mössbauer nucleus and the main component V_{zz} of the electric-field gradient (EFG) acting on the nucleus. The EFG is the gradient of the electric field $\nabla\nabla V$ expressed as a tensor quantity consisting of three non-zero terms $\frac{\partial^2 V}{\partial x^2} \equiv V_{xx}$, $\frac{\partial^2 V}{\partial y^2} \equiv V_{yy}$ and $\frac{\partial^2 V}{\partial z^2} \equiv V_{zz}$, with axes chosen to achieve $|V_{zz}| \geq |V_{yy}| \geq |V_{xx}|$. As these three partial derivatives are not independent due to $\nabla^2 V = 0$ (Laplace's equation), V_{zz} and η are chosen as the minimum set of parameters characterizing the EFG:

$$\eta = \frac{|V_{xx} - V_{yy}|}{|V_{zz}|} \tag{1}$$

There are two major contributors to the EFG: The oxygen anions surrounding the Fe atom (ligand contribution, V_{zz}^{ligand}) and the ordered d orbitals of Fe^{2+} (orbital-ordering contribution, V_{zz}^{OO}), both approximated as point charges. The calculation details have been described previously [19,20]. Atomic coordinates from Ref. [11] were used to estimate V_{zz}^{ligand} for the charge-ordered Fe^{2+} and Fe^{3+} as well as for valence-mixed $Fe^{2.5+}$. The EFG constants are listed in Table 2.

Calculations of the internal field. The measured internal magnetic field B of an iron component in $YBaFe_2O_5$ is a sum of three collinear vectors, the lengths of which add as:

$$-B = -B_{\text{FC}} + B_{\text{dip}} + B_L, \tag{2}$$

where B_{FC} is the Fermi-contact field proportional to the spin of the iron atom, B_{dip} is the dipolar field of the minority-spin electron of the Fe^{2+} parentage (the underlying high-spin d^5 configuration does not produce any dipolar field), and B_L is the orbital field. The dominant B_{FC} is summed with negative sign to emphasize that Fermi-contact interaction inverts the direction of the field when observed by the nucleus. The dipolar fields for the individual d orbitals occupied by a sole electron of spin along b (direction as in Ref. [11]) are listed in Table 2.

Table 2
Contributions to EFG and dipolar field B_{dip} at the Mössbauer nucleus of the generic $RBaFe_2O_5$ [19,21] (R=rare earth) from iron d orbitals and oxygen ligands.

	d_{xy}	d_{xz}	d_{yz}	$d_{x^2-y^2}$	d_{z^2}	Fe^{2+}_{ligand}	Fe^{3+}_{ligand}	$Fe^{2.5+}_{\text{ligand}}$
B_{dip} (T)	−17	34	−17	−17	17	–	–	–
eQV_{xx} (mm/s)	−2.4	−2.4	4.8	−2.4	2.4	−0.15	−0.36	−0.49
eQV_{yy} (mm/s)	−2.4	4.8	−2.4	−2.4	2.4	−0.87	−0.38	−0.51
eQV_{zz} (mm/s)	4.8	−2.4	−2.4	4.8	−4.8	1.02	0.74	1.00

A comparison of the fields in Table 2 shows that d_{xy} and $d_{x^2-y^2}$ give identical contributions to B_{dip} and EFG, and, on this basis alone, these two orbitals cannot be discerned. Similarly, d_{yz} and d_{xz} together have the same effect as d_{z^2} alone. Accordingly, only three orbitals, $d_{xz}/d_{x^2-y^2}$, d_{z^2} and d_{xz}/d_{yz}, represent the linearly independent set to model hyperfine parameters. We have chosen $d_{x^2-y^2}$, d_{z^2} and d_{xz} identified in the DFT study of $YBaFe_2O_5$ [16] as having highest occupancies of the minority-spin electron. The results for the alternative set where d_{xy} replaces $d_{x^2-y^2}$ are presented in the Supporting Material.

Minority-spin occupancies and refining B and V_{zz}. Each iron state manifested as a Mössbauer component in the spectrum has its characteristic minority-spin electron populations $n_{x^2-y^2}$, n_{z^2} and n_{xz} in the respective d orbitals. In the valence-mixed state, also n_{yz} had to be used to prevent negative populations (Section 4.6.1). With Table 2, Eqs. (3) were set up to link the observed EFG and the internal field to the orbital occupancies:

$$n_{x^2-y^2} + n_{z^2} + n_{xz} = p \tag{3a}$$

$$-17n_{x^2-y^2} + 17n_{z^2} + 34n_{xz} - B_{\text{FC}}\tfrac{5-p}{5} + pB_L = -B^0 \tag{3b}$$

$$-2.4n_{x^2-y^2} + 2.4n_{z^2} - 2.4n_{xz} + eQV_{xx}^{\text{ligand}} = eQV_{xx} \tag{3c}$$

$$-2.4n_{x^2-y^2} + 2.4n_{z^2} + 4.8n_{xz} + eQV_{yy}^{\text{ligand}} = eQV_{yy} \tag{3d}$$

$$4.8n_{x^2-y^2} - 4.8n_{z^2} - 2.4n_{xz} + eQV_{zz}^{\text{ligand}} = eQV_{zz} \tag{3e}$$

where $0 \leq p \leq 1$ is the total minority-spin electron population determined from the iron valence of the Mössbauer component. The values V_{xx} and V_{yy} were determined from the measured V_{zz} and η by combining $\nabla^2 V = 0$ with Eq. (1). The orbital field B_L is a value corresponding to the angular momentum this component can carry per unit of minority-spin electron. The Fermi-contact field B_{FC} is a spin-only value for $S = 5/2$ and the factor $\frac{5-p}{5}$ converts it into the Fermi-contact field for the actual p of the Mössbauer component. B^0 is the component's temperature-corrected hyperfine field. The sign convention is the same as in Eq. (2).

Eqs. (3) form a redundant set. Only the two first equalities are needed together with one of the three latter for the EFG, depending on the identification of the main (largest) EFG component V_{zz}: Its angle β to B is set tentatively to 0 or 90°, and the third equation is chosen so that, within error margins, the obtained $n_{x^2-y^2}$, n_{z^2} and n_{xz} populations are not negative and yield $|V_{xx}|$, $|V_{yy}| \leq |V_{zz}|$, avoiding thus "population violations" and "EFG violations", resp. When $\beta = 0$, the second and fourth equality of the set of Eqs. (3) become linearly dependent, and either the third or fifth equality must be used. The right-hand side values V_{xx} or V_{yy} then need to be calculated from V_{zz} and η with the same consistency check as above.

As verified previously on a generalized d-wavefunction model [20], B_L is introduced as a free parameter expressing the angular momentum along the spin direction due to the minority-spin electron occupancy in d_{xz}, $d_{x^2-y^2}$, and $d_{z^2} \equiv -(d_{x^2-z^2} + d_{y^2-z^2})/\sqrt{3}$, implying them as degener-

ate. Occupancies of $d_{x^2-y^2}$ and d_{z^2} combine into $d_{x^2-z^2}$, with which d_{xz} of the same symmetry yields an angular momentum along y. This is expressed with the minority-spin electron populations η as a complex linear combination $\sqrt{n_{xz}}d_{xz} \pm i(\sqrt{n_{x^2-y^2}}d_{x^2-y^2} - \sqrt{n_{z^2}}\,d_{z^2})$. The population n_{yz} does not contribute since the symmetry-related partner, d_{xy}, is not occupied by the minority-spin electron; $d_{x^2-y^2}$ is, according to Ref. [16]. The orbital field along y due to the minority-spin electron fraction p at the Fe atom is then $p|B_L| = 2B_L^0(\sqrt{n_{x^2-y^2}n_{xz}} + \sqrt{3n_{z^2}n_{xz}})$, where the B_L^0 parameter to be determined relates orbital field to angular momentum. The results for the alternative set of orbitals in which d_{xy} replaces $d_{x^2-y^2}$ are in the Supporting Material.

Upon sharing a portion of the Fe minority-spin electron between the more divalent parent component and its more trivalent counterpart, angular momentum must be conserved. The total angular momentum L_y^{tot} of that electron is therefore controlled by the smaller of the two local angular momenta pL_y^{tot}. The B_L of the minority-spin electron is then:

$$|B_L| = \frac{2B_L^0}{p_c}\left[\sqrt{n_{(x^2-y^2)c}n_{(xz)c}} + \sqrt{3n_{(z^2)c}n_{(xz)c}}\right], \quad (6)$$

where $n_{(x^2-y^2)c}$, $n_{(z^2)c}$, $n_{(xz)c}$, and p_c concern the "controlling" Mössbauer component whereas n and p in the set of Eqs. (3) refer to the component for which the set is actually being expressed.

4. Results

4.1. Stoichiometry optimization

Since quenching from 1000 °C at $\log(p_{O_2}/\text{bar}) = -15.56$ yields product containing metallic iron, Fig. 3 suggests $w = 0.015$ for the lower nonstoichiometry limit in $YBaFe_2O_{5+w}$. Equilibrium with iron foil at 450 °C yields $YBaFe_2O_{5.012}$ when quenched and $YBaFe_2O_{5.015}$ when slowly cooled. The *Pmma* unit-cell parameters at 295 °C of the latter two samples are $a = 8.0150(1)$, $b = 3.8541(0)$, $c = 7.5530(1)$ Å and $a = 8.0152(1)$, $b = 3.8543(0)$, $c = 7.5533(1)$ Å, respectively; the values for quenched samples are in Fig. 4.

4.2. DSC across the valence-mixing transitions

The strong endothermic event in Fig. 5 at T_V is the discontinuous Verwey transition of volume change and phase coexistence [11,17]. The weaker second transition tops at T_p. The transition parameters are in Table 3. The total transition entropies for the two samples annealed with iron foil are $\Delta S = 8.6$ for the slowly cooled sample and

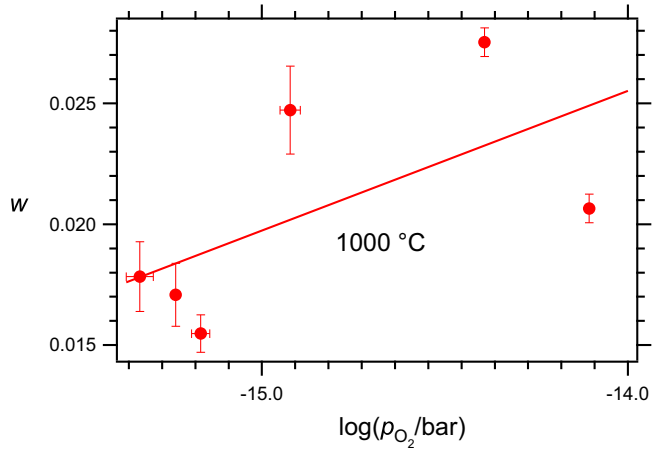

Fig. 3. Oxygen nonstoichiometry w of $YBaFe_2O_{5+w}$ quenched from equilibrium with atmospheres of controlled p_{O_2} at 1000 °C. Quenching from $\log(p_{O_2}/\text{bar}) = -15.56$ and −15.66 yielded partially and fully decomposed perovskite, resp., upon appearance of metallic Fe.

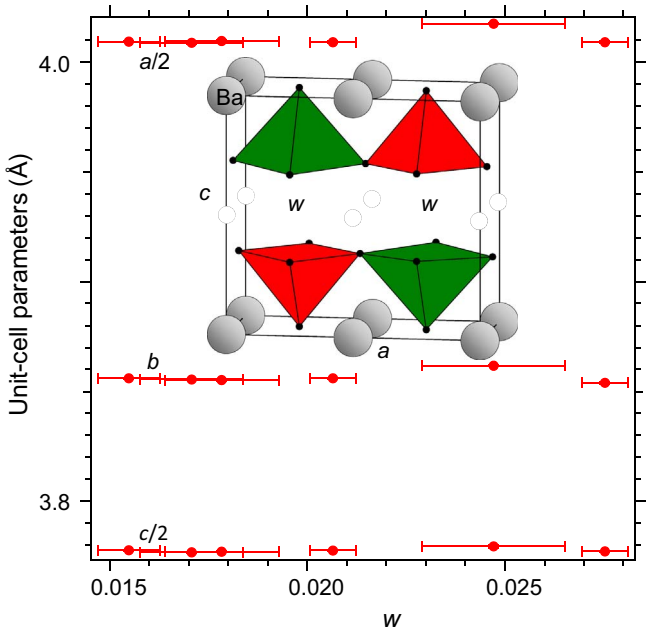

Fig. 4. The unit cell and its room-temperature parameters for $YBaFe_2O_{5+w}$ quenched from equilibrium with atmospheres of controlled p_{O_2} at 1000 °C. The coordination polyhedron of oxygens around divalent iron is in green, trivalent in red.

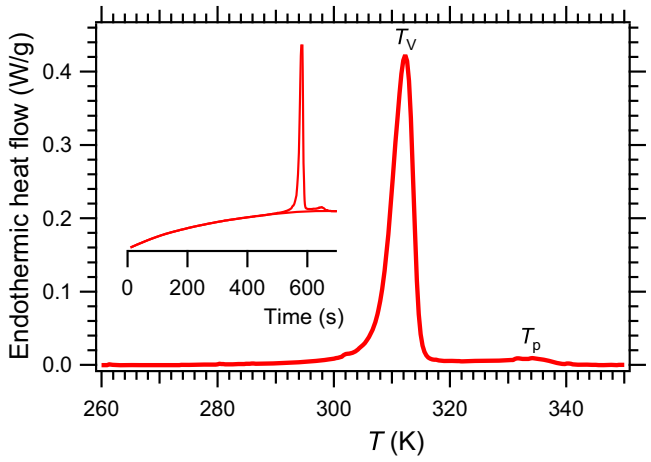

Fig. 5. DSC endothermic effects upon heating $YBaFe_2O_{5.012}$ at 20 K/min, with background subtraction illustrated in the inset.

Table 3
Thermodynamics of the two valence-mixing transitions upon heating $YBaFe_2O_{5.012}$ at zero rate.

Parameter for transition	Main	Second	Total
T_c (K) peak top	311	334	
ΔS ($\text{Jmol}^{-1}\text{K}^{-1}$)	8.40	0.6	9.0

9.0 $\text{Jmol}^{-1}\text{K}^{-1}$ for the quenched one. This is within the scatter 8.9 ± 0.4 for 10 measurements of 4 samples of lowest nonstoichiometry quenched from 1000 °C. The main transition has hysteresis of about 4 K (Fig. 6) while T_p shows no hysteresis.

4.3. Mössbauer spectra across all transitions

Spectra typical of the charge-ordered, intermediate and valence-mixed AFM iron states below T_N in $YBaFe_2O_{5.012}$ (quenched from 450 °C) are in Fig. 7. The spectrum recorded above T_N is in Fig. 8

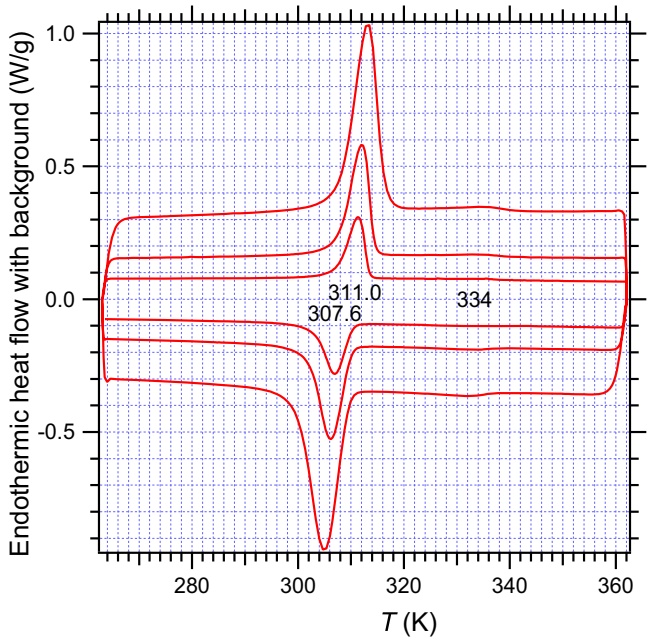

Fig. 6. Sequential DSC scans of $YBaFe_2O_{5.012}$ upon cooling and heating rate of 40, 20 and 10 K/min for hysteresis evaluation (linear extrapolation leads to zero-rate temperatures listed in the middle).

and has a single peak of valence-mixed iron (a very narrow paramagnetic doublet) and a weak paramagnetic doublet of Fe^{3+}. The latter is due to the non-zero limit in $YBaFe_2O_{5+w}$ nonstoichiometry w, which introduces a small excess of trivalent iron, possibly enhanced by oxidation.

While only the long-range charge order of $YBaFe_2O_5$ is seen by diffraction methods [11], Mössbauer spectra have the complementary local resolution. Just as diffraction sees two phases in equilibrium in the middle of the main Verwey transition, Mössbauer spectra show the charge-ordered and intermediate component pairs coexisting. Since the transition at T_p is invisible to diffraction, only Mössbauer spectra reveal a similar coexistence of intermediate and valence-mixed Fe pairs. Fig. 9 shows the content of these three Fe pairs across the two transitions. The final valence mixing appears in small extent right above T_V, when the intermediate components are approaching their maximum intensity, and shoots up when they disappear precipitously at T_p. The ranges where the two component pairs coexist are practically not affected by the thermal history of the sample, and neither is T_V (Fig. 10). An overview of the thermally induced merging of the two iron valences is shown in Fig. 11, derived from temperature-corrected Mössbauer center shifts as described in Section 3.

4.4. Mössbauer components

4.4.1. Charge-ordered pair

Charge-ordered Fe^{2+} has an internal field ~7.5 T (Fig. 12), typical also for other rare-earth variants of $YBaFe_2O_5$ [13,24–26], where the large dipolar field of the minority-spin electron in d_{xz} nearly cancels the Fermi-contact field. This same electron makes the EFG large (Fig. 13), despite a small negative contribution from oxygen ligands (Table 2, row for eQV_{yy}), and both η and eQV_{zz} can be fitted simultaneously.

Charge-ordered Fe^{3+} of centrosymmetric d^5 configuration has an internal field equal to the Fermi-contact field and a quadrupole-coupling constant defined by the ligand contribution. Extrapolation of the internal field to 0 K yields $B_{FC} = 51.93$ T (Fig. 2) used directly when solving Eqs. (3). Compared to internal field, the quadrupole-coupling constant has only a minor effect on the spectrum fit since V_{zz} is rather small and perpendicular to the field: When η is fixed to zero, eQV_{zz} is smaller than the ligand $eQV_{zz} = 0.74$ mm/s expected from Table 2. We decided to refine η and eQV_{zz} simultaneously in the fit, yielding somewhat scattered values for both, but of the correct order (Fig. 13). The Fe^{3+} intensity represents ~52% of the component pair. This is not due to the oxygen excess w (such an octahedrally-

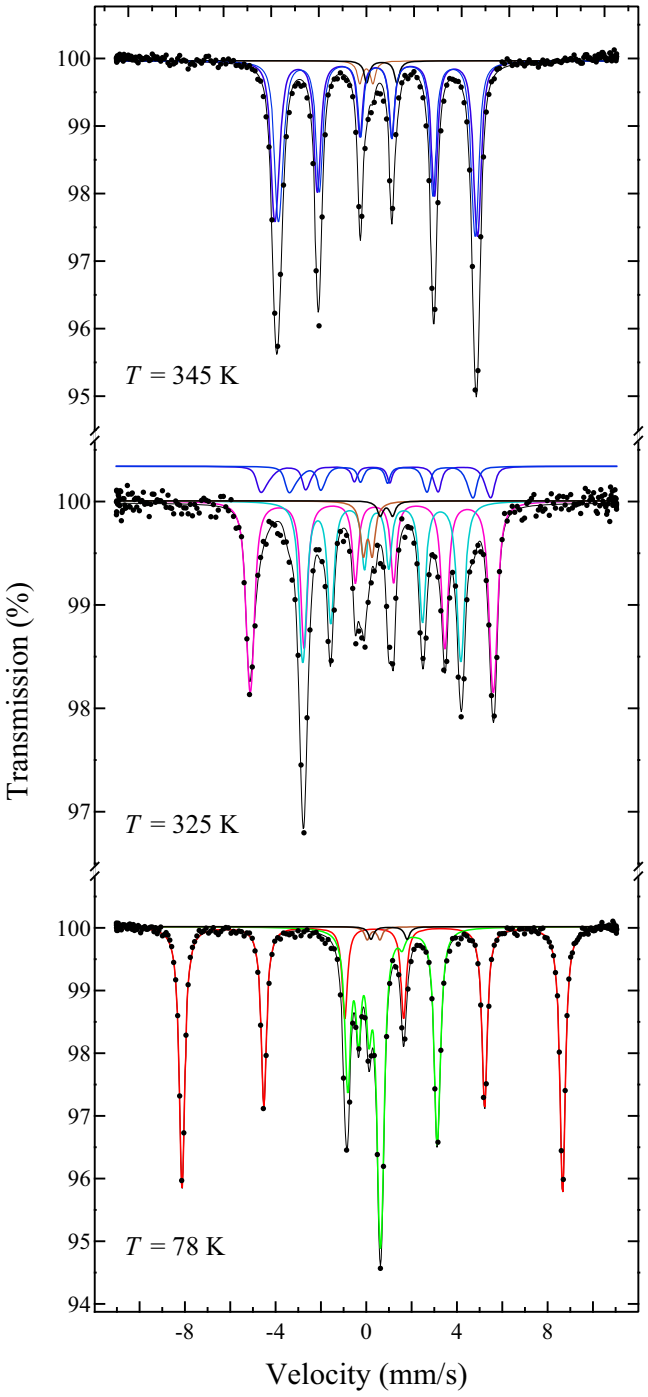

Fig. 7. ^{57}Fe Mössbauer spectra of quenched $YBaFe_2O_{5.012}$ as valence mixed (345 K), partially valence mixed (325 K) and charge ordered (78 K). The main di- and trivalent components are drawn in green and red, the respective intermediate components in cyan and magenta, the valence-mixed components in blue (and shifted in the middle spectrum for clarity). Two components argued to be due to domain walls (DW) are drawn in brown (the trivalent counterpart) and black (the divalent counterpart). (For interpretation of the references to color in this figure legend, the reader is referred to the web version of this article.)

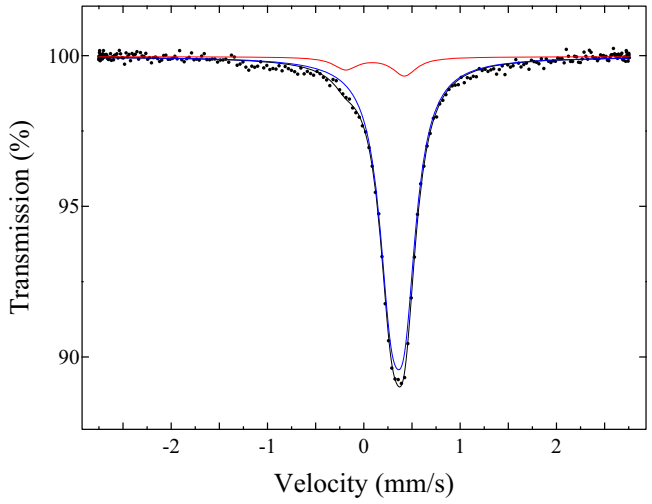

Fig. 8. Mössbauer spectrum of paramagnetic $YBaFe_2O_{5.017}$ at 448 K with valence-mixed component (blue unresolved doublet) and trivalent Fe (red doublet). (For interpretation of the references to color in this figure legend, the reader is referred to the web version of this article.)

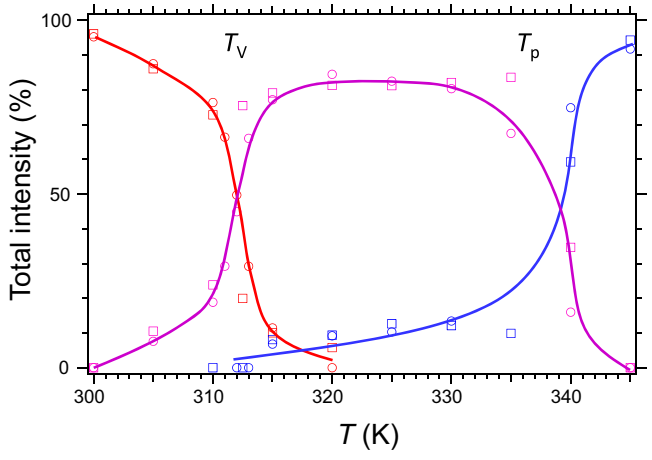

Fig. 9. Evolution across the two transitions of the total Mössbauer intensities for the charge-ordered pair (red), intermediate pair (magenta) and valence-mixed pair (blue) in $YBaFe_2O_5$ annealed at 450 °C and quenched (□$YBaFe_2O_{5.012}$) or slowly cooled (◯$YBaFe_2O_{5.015}$). Lines are drawn as guide for eye. (For interpretation of the references to color in this figure legend, the reader is referred to the web version of this article.)

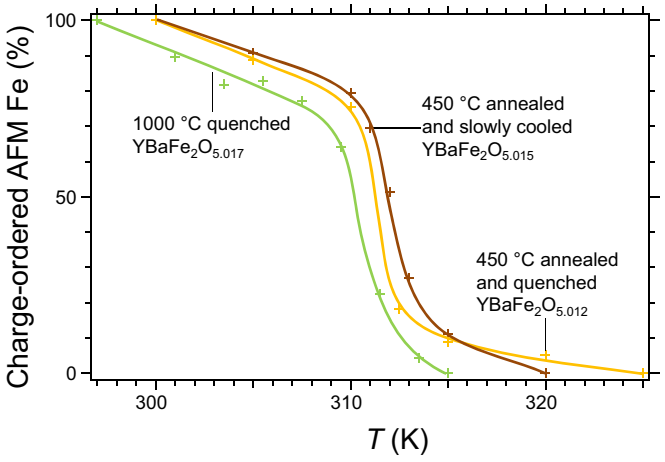

Fig. 10. Conversion of the charge-ordered component of the Mössbauer spectrum for the three $YBaFe_2O_5$ samples of different thermal history. The same T_V sequence was observed by DSC measurements: 310.5, 311.0 and 311.2 K.

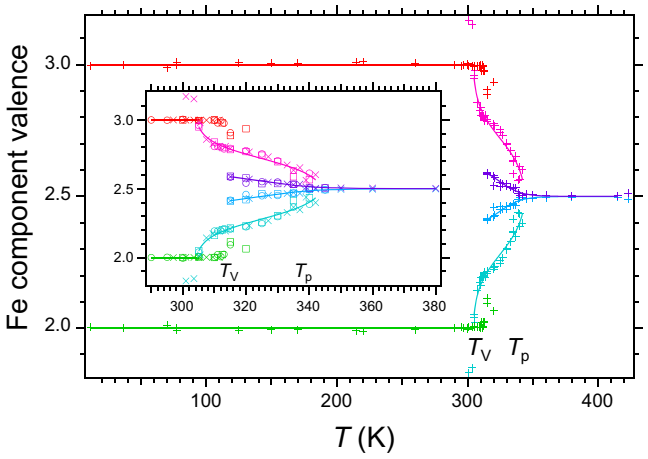

Fig. 11. Temperature evolution of iron valences in charge-ordered (green and red), intermediate (cyan and magenta) and valence-mixed (blue) $YBaFe_2O_5$. The detail in the inset identifies thermal history: quenched from 1000 °C (×$YBaFe_2O_{5.017}$), annealed at 450 °C and quenched (□$YBaFe_2O_{5.012}$), annealed at 450 °C and slowly cooled (◯$YBaFe_2O_{5.015}$). (For interpretation of the references to color in this figure legend, the reader is referred to the web version of this article.)

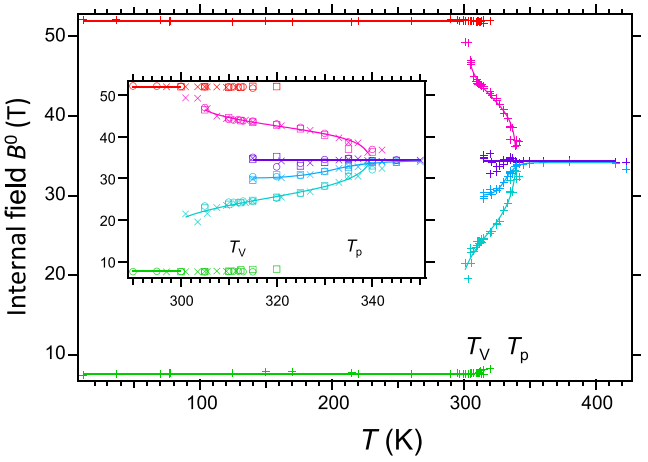

Fig. 12. Temperature evolution of B^0 that reflects the pure effect of valence mixing in $YBaFe_2O_5$. The inset identifies thermal history: quenched (×$YBaFe_2O_{5.017}$), annealed and quenched (□$YBaFe_2O_{5.012}$), annealed and slowly cooled (◯$YBaFe_2O_{5.015}$).

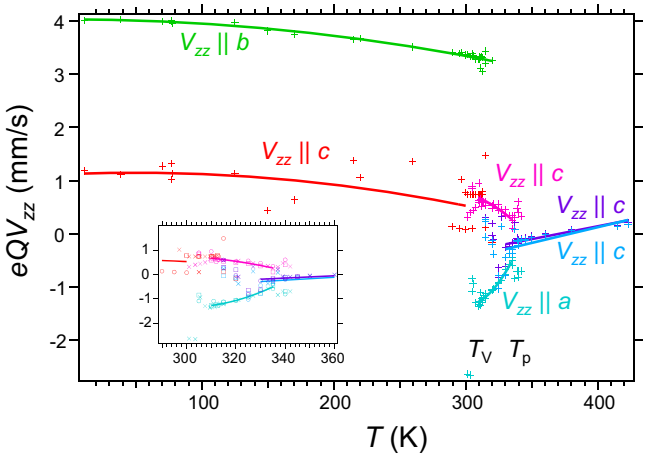

Fig. 13. Evolution of eQV_{zz} in $YBaFe_2O_5$ from charge ordered (green and red) to intermediate (cyan and magenta) and valence mixed (blue). The inset identifies thermal history: quenched (×$YBaFe_2O_{5.017}$), annealed and quenched (□$YBaFe_2O_{5.012}$), annealed and slowly cooled (◯$YBaFe_2O_{5.015}$). (For interpretation of the references to color in this figure legend, the reader is referred to the web version of this article.)

coordinated component would have a somewhat larger internal field) but due to high Debye temperature $\Theta_D = 532$ K for Fe^{3+} of short bonds, versus 289 K for the larger Fe^{2+} (Fig. 1). The probability of Mössbauer absorption is given by the fraction f of recoilless absorption of Mössbauer γ-ray quanta, which in turn depends on Θ_D. The low-temperature limit of the f factor is given by [27],

$$f = \exp\left[-\frac{E_R}{k_B\Theta_D}\left(\frac{3}{2}+\frac{\pi^2T^2}{\Theta_D^2}\right)\right], \quad (7)$$

where $E_R = 1.95$ meV is the recoil energy of a free ^{57}Fe atom and k_B is the Boltzmann constant. Assuming that the difference in the intensity of the Mössbauer components at 77 K is only due to the recoil-free fraction f, 52.5% of Fe^{3+} (47.5% of Fe^{2+}) is predicted; in accord with what is seen.

The dedicated fit of the spectrum had to deal with asymmetric line broadening close to T_V when the divalent component broadens more than the trivalent one. The broadening was parametrized with one single halfwidth Δp_P of a narrow one-sided Poisson distribution from the 2+ and 3+ limits towards the average Fe valence. As the temperature approaches T_V, a tiny minority-spin electron fraction appears at Fe^{3+}, in a first approximation distributed equally over the t_{2g} orbitals, with equal Δp_P. Such a partial electron transfer affects the hyperfine parameters asymmetrically: in Fe^{3+} the Fermi-contact field B_{FC} changes, in Fe^{2+} both B_{FC} and B_{dip} do. In Fe^{3+} the quadrupole coupling constant is unaffected, in Fe^{2+} the orbital contribution to eQV_{zz} changes (cf. Eqs. (3)). The Fe^{3+} and Fe^{2+} sextets then approach each other by a small isomer-shift change $\Delta\delta$ (mm/s) that can be obtained by linear interpolation of the actual halfwidth Δp_P on the isomer-shift scale that represents 1 valence unit, $0.5262 = 0.9753 - 0.4491$, when extrapolated to 0 K in Fig. 1:

$$\Delta\delta = \pm 0.5262\Delta p_P \quad (8)$$

4.4.2. Intermediate pair

At T_V, the emerging intermediate component of divalent parentage has internal field of 24 T and negative eQV_{zz} along the a axis [21]. Its trivalent companion has an internal field of 44 T and a positive eQV_{zz} (along c, like for $NdBaFe_2O_5$ [20] and $GdBaFe_2O_5$ [21]) due to ligands, with a minor contribution from d_{z^2} and $d_{x^2-y^2}$, both having V_{zz} along c.

The spectrum fit was done in two steps. In the first step, broadening beyond the natural linewidth was modeled by ΔB to yield hyperfine parameters from which the populations $n_{x^2-y^2}$, n_{z^2} and n_{xz} at each iron component were evaluated. In the second step, Gaussian distribution of their sum p was used instead of the ΔB (the valences inside the +2 to +3 interval imply Gaussian rather than Poisson-like broadening). The obtained distribution peak was then scaled by the fractional populations $n_{x^2-y^2}$, n_{z^2} and n_{xz} to obtain the orbital Gaussian populations that generate via Eqs. (3) the distributions of the hyperfine parameters to fit the spectrum. The isomer-shift values were calculated with Eq. (8) using Δp_G instead of Δp_P. Furthermore, the intensities of the intermediate pair were constrained equal in the vicinity of T_p where these two components disappear precipitously.

In general, the parameters Δp_G, Γ and ΔB tend to correlate, and the fit relies on subtle differences: The linewidth Γ refers to all components by adjusting the width of all resonance lines identically. The internal-field distribution ΔB causes deviation from the typical 3 : 2 : 1 : 1 : 2 : 3 powder sample [27] peak-height ratio in the sextet because it broadens more the outer than the inner lines while maintaining the peak-area ratio 3 : 2 : 1 : 1 : 2 : 3. The valence distribution halfwidth Δp_G not only broadens the lines, but makes the sextet asymmetric by linking the internal field, quadrupole coupling and isomer shift together via the electron distribution it implies.

4.4.3. Valence-mixed pair

While initially separated by ~6 T above T_V, the internal fields of the two valence-mixed components become almost equal at T_p and gradually merge towards T_N, in the vicinity of which the fit is no longer precise (Fig. 12). When averaged, their temperature evolution yields $T_N = 433(1)$ K via least-squares fit with Brillouin function (Fig 2), in agreement with 432 K for $HoBaFe_2O_5$ obtained from the decay of the ordered moment seen by neutron powder diffraction [18]. An analogous fit of the center shifts yields a Debye temperature of 629 K (Fig. 1), larger than Θ_D for the charge-ordered components due to volume contraction observed by X-ray diffraction [11] at T_V and manifested also in a Mössbauer-absorption change shown in Fig. 14. In general, quadrupole coupling constants are close to zero, and isomer shifts remain very close to the arithmetic average of the charge-ordered pair.

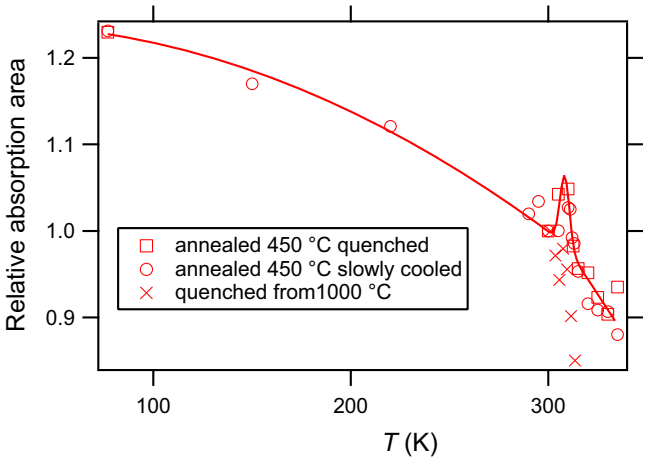

Fig. 14. Absorption area relative to the 300 K value of Mössbauer spectra for $YBaFe_2O_{5.015(3)}$ of different thermal history. Least-squares fit as a guide for eye emphasizes an absorption peak at T_V where the temperature dependences change slope. The peak can be traced in all measurements shown, even if the three data sets overlap poorly.

The two valence-mixed components in the spectrum were fitted in two steps with their intensities constrained equal. In the first step, each of the two components had its own independent internal field, center shift and quadrupole-coupling constant; yielding its populations $n_{x^2-y^2}$, n_{z^2}, n_{xz} and n_{yz} that sum up to the p of the component. In the second step, the two populations for each orbital were averaged, and the two sets of hyperfine parameters to actually fit the spectrum were calculated from two populations generated around the average as a symmetrical split. The width of the split, used as a fit variable, is equal to the order parameter $|2(p - 0.5)|$. Gaussian halfwidths for the minority-spin electron content distribution Δp_G were used to fit the observed asymmetric broadening.

Using one single set of hyperfine and valence parameters for both valence-mixed components ascertained that changes in their hyperfine parameters could only evolve in a correlated manner in the second fit. This was needed when the valence-mixed intensities were low below T_p and also when the overlap of the two components increased upon increasing temperature. The Gaussian broadening Δp_G was high around T_p where the intermediate and valence-mixed components' intensities change rapidly and unevenly across the sample in the narrow temperature interval, and it increased again as T_N was approached and AFM interactions were vanishing upon broadening and disappearance of the spectral sextet.

4.5. Planar defects

All Mössbauer spectra of $YBaFe_2O_5$ below T_N have a small practically paramagnetic component of isomer shift ~0.1 mm/s close to trivalent Fe, showing increased intensity above T_V. The origin of this component has not yet been clarified. It is not seen by X-ray diffraction

as an impurity phase. Neither is it surface related, as the conversion-electron Mössbauer spectra probing the surface layer into a depth of about 100 nm of the powder sample do not show increased amounts of this component [present authors, unpublished]. After all AFM components have been carefully modeled by the mixed-valence fit (vide supra), adding also a divalent paramagnetic companion of equal concentration improves the fit, with its isomer shifts refining to 0.6–1.0 mm/s. The isomer shifts of the two paramagnetic components then follow better the expected thermal Debye behavior; eliminating erratic variations for just one component.

The two symmetry-changing transitions at T_N and T_V are likely to generate extended defects: domain walls upon spin ordering at T_N and antiphase boundaries upon charge ordering at T_V. Cooling through T_N makes numerous seed points to expand their AFM patterns to eventually form domain walls where wrong moments meet and then rotate to relieve the frustration. That yields local magnetic fields much smaller than in the bulk [28]. Cooling through T_V is bound to generate antiphase-boundary defects of Fe ions of the same charge, which would clamp to the already present domain walls.

In the valence-mixed state below T_N, the wrong moments to meet at the *ab*-plane domain wall are antiparallel, because the Fe–Fe coupling across the Y layer is FM. Upon cooling through T_V, these *ab*-plane domain walls disappear as all FM couplings become AFM [13]. As their Fe atoms are ready to join the charge order, the total concentration of the planar-defect components decreases to about 2/3 below T_V.

Unexpectedly, the concentrations of the planar-defect components do not change much with the tested variations of the sample thermal history. In fact, the slowly cooled $YBaFe_2O_5$ has a little more of them. This might be due to more seeds being available upon slow cooling of the polycrystalline sample.

4.6. Solving the set of Eqs. (3) into occupancies

The set of Eqs. (3) was solved for each point of the temperature-evolution curves of iron valences in Fig. 11, of B^0 in Fig 12, and of V_{zz} in Fig. 13, which at most temperatures kept Eqs. (3a)–(3e) linearly independent. When possible, we tried to avoid η as a parameter because it depends on the difference of V_{xx} and V_{yy} (Eq. (1)), hence any error in point-charge estimates used in our EFG model amplifies the errors of η entered into Eqs. (3). No temperature evolution was assumed in the charge-ordered state below T_V, and the set was solved for the temperature 20 K where precise crystal-structure data exist [11]. Accordingly, a small temperature dependence for eQV_{zz} of Fe^{2+} in Fig. 13 was not considered because it is likely to be due to anisotropic thermal expansion of the structural coordination polyhedra made conspicuous by the high T_V of $YBaFe_2O_5$.

When the ambiguity between the direction and sign of V_{zz} was encountered, all combinations were tested to achieve self-consistency. Since V_{zz} of charge-ordered Fe^{2+} is along *b* and the magnetic moments too [13,24–26], their angle $\beta = 0°$, and η (Eq. (1)) is needed to evaluate eQV_{yy} so that Eqs. (3) remain linearly independent. Usually η affects the Mössbauer spectrum very weakly, but for charge-ordered Fe^{2+}, the dependence is stronger as the electric and magnetic hyperfine interactions are of similar large magnitude. In the charge-ordered state, there are no free parameters, since B_L is zero for both Fe species. Fitting the spectrum with two DW/APB components yields $\eta \approx 0.50$ in better agreement with η estimated via Eq. (1) from values in Table 2 for the Fe^{2+} population $n_{xz} = 1$: $\eta = [(1.02 - 2.4) - (-0.15 - 2.4)]/(4.8 - 0.87) = 0.297$. In contrast, a single paramagnetic component yields $\eta \approx 0.7$.

The set of Eqs. (3) was solved iteratively for a seeded B_L and a fixed $B_{FC} = 51.93$ T. After each iteration step, B_L was recalculated with Eq. (6) for both Fe components, and the smaller B_L of the two was chosen. The parameter B_L^0 was fixed at 10.0 T because there is an interval about it that is not causing population violations. When $B_L^0 = 10.0$ T, the largest possible value for the orbital field B_L is 20 T for a single electron of $p_c = 1$ in Eq. (6) and occupancies $n_{(x^2-y^2)c} = 1/8$, $n_{(z^2)c} = 3/8$, $n_{(xz)c} = 1/2$. Given the gyromagnetic ratio 2 of an electron's magnetic dipole moment to its angular momentum, the B_L maximum of 20 T is assuringly close to one half of the spin dipolar field for a single d_{xz} electron in Table 2. In order to make the iteration stable, the B_L update after each step was done by mixing only a fraction of the new value with the old one and by repeating the iteration until no changes were detected in the populations and B_L, provided all populations obtained were positive. As already mentioned, for the valence-mixed components, the population n_{yz} had to be added as a fourth variable. This is described in more detail in the following, together with the procedure we adopted to establish the EFG direction when V_{zz} was small.

4.6.1. Implications for EFG above T_p

The quadrupole-coupling constants above T_p are close to zero. This means that all components of the EFG should be close to zero because $|V_{zz}|$ is per definition the largest of them. Analyzing the Mössbauer spectra upon assumption of $\beta = 90°$ suggests that V_{zz} is either along the *a* or *c* axis. Attempts to fit the spectra with $\beta = 0°$ yielded even smaller quadrupole-coupling constants, along with a sign inversion. This situation could not be reproduced in the population analyses and was abandoned. Positive populations could be obtained for both orientations allowed by $\beta = 90°$, but with EFG violations ($|V_{zz}|$ not being the largest along a temperature interval). The violations were dealt with by allowing the valence-mixed component to populate also the d_{yz} orbital of energy almost as low as d_{xz} above T_V due to the fading orthorhombic distortion. Whereas for V_{zz} along *a* this did not help, setting V_{zz} along *c* almost completely removed the EFG violations and made $|V_{zz}|$ largest.

Since the introduction of n_{yz} makes the set of Eqs. (3) linearly dependent, we applied the conditions that $0 < n_{yz} \leq n_{xz}$ due to orbital energy and that $V_{xx} = V_{yy} = 0$ since $V_{zz} = 0$. Empirical fit yielded $n_{yz} \approx 0.87 n_{xz}$ that gives non-violating EFG for valence-mixed components at all temperatures.

Above $T_N = 433$ K, the equality for the internal field disappears from the set of Eqs. (3). Considering the smooth evolution above T_p towards the small positive eQV_{zz} of the valence-mixed phase, the orbital populations can be extrapolated into the paramagnetic phase at T_N. However, the actual mathematical solution is no longer unique there, as several combinations of the four populations together with the ligand EFG can produce the same experimental eQV_{zz}.

4.6.2. Implications for orbital field B_L

Thermal evolution of B_L obtained through the iterative process is shown in Fig. 15. In the charge-ordered phase, the AFM coupling between the charge-ordered Fe pair prevents minority-spin electron

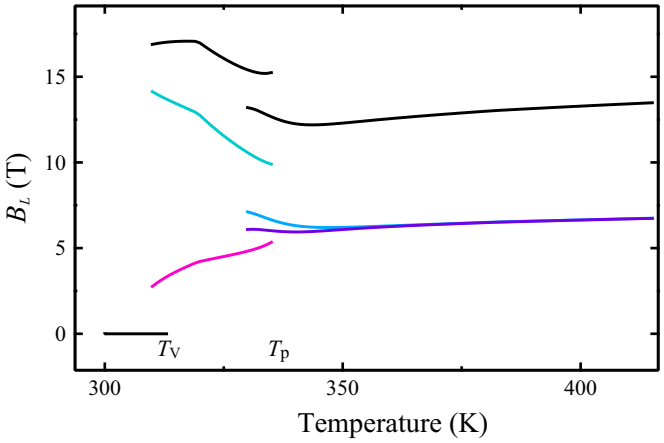

Fig. 15. Estimated orbital field B_L for the minority-spin electron total (black) and its break up into the two iron-site valences of the intermediate state (cyan $Fe^{<2.5+}$ and magenta $Fe^{>2.5+}$) and valence-mixed state (blue color added). (For interpretation of the references to color in this figure legend, the reader is referred to the web version of this article.)

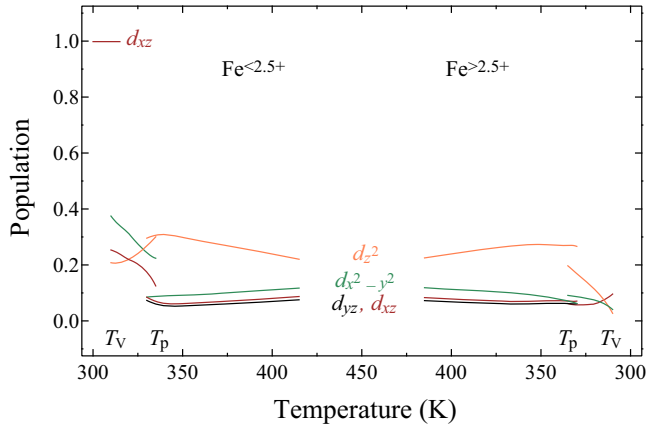

Fig. 16. Temperature evolution (towards the plot center) of calculated (Eqs. (3)) non-zero minority-spin populations in $d_{x^2-y^2}$, d_{z^2} and d_{xz} orbitals of the components of divalent (left) and trivalent (right) parentage, as they occur in the charge-ordered, intermediate and valence-mixed regions of the $YBaFe_2O_5$ sample, upon thermally induced mixing towards the paramagnetic fully valence-mixed state. The additional d_{yz} population concerns the valence-mixed components only. The tiny minority-spin electron presence at the charge-ordered trivalent Fe around T_V is neglected as discussed in Section 4.6.

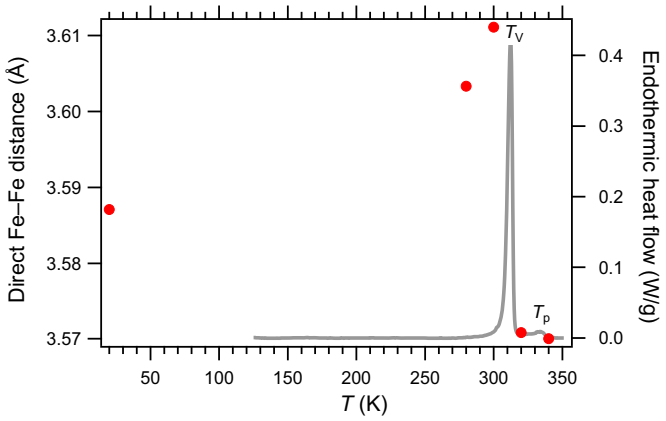

Fig. 17. Temperature evolution of the direct Fe–Fe distances (red dots) [11] follows the valence mixing manifested by the entropy supplied as DSC heat (gray line). The shortest Fe–Fe distance in Fe metal is 2.48 Å.

transfers below T_V. The B_L is zero because the doubly occupied d_{xz} orbital of Fe^{2+} has no degenerate partner for the minority-spin electron to produce angular momentum along the spin direction. Above T_V, both Fe species begin to distribute the minority-spin electron over d_{xz}, d_{z^2} and $d_{x^2-y^2}$, and a non-zero B_L arises in accord with Eq. (6). Upon their thermally induced electron sharing, the two iron components approach each other to merge their nearly constant B_L at full mixing.

5. Discussion

The calculated $d_{x^2-y^2}$, d_{z^2}, d_{xz}, and d_{yz} populations are shown in Fig. 16. As inferred in Ref. [11] from the crystal structure of charge-ordered $YBaFe_2O_5$, the minority-spin electron at low temperatures occupies the d_{xz} orbitals which then stack along the strings of Fe^{2+} that form a checkerboard with strings of Fe^{3+} (Fig. 4) in a lattice contracted along the string direction.

Upon heating through the Verwey transition, 93% of mixing entropy is supplied to these two ions, and the minority-spin electron relocates mainly into $d_{x^2-y^2}$ (besides d_{xz} and d_{z^2}). Note that replacing $d_{x^2-y^2}$ with d_{xy} in an alternative set of orbitals yields qualitatively the same result (Supplementary Material). The orbital symmetry thus justifies the intermittent checkerboard order of charges indicated by modulation of the magnetic moment in a combined X-ray and neutron-diffraction study of a $TbBaFe_2O_5$ single crystal [29]. This coulombic order is very weak since it prevails when mere 7% of entropy is missing to fully mix the charges.

At T_p, the remaining entropy is supplied, the charge order disappears, and d_{z^2} orbitals dominate. As neither these d_{z^2} nor the $d_{x^2-y^2}$ of the intermediate state are favored in a square-pyramidal ligand field, their occupancy above T_V suggests a weak direct Fe–Fe interaction that lowers their energies. Fig. 17 shows that the entropy gain upon heating through T_V and T_p (a measure of valence mixing) is proportional to shortening of the Fe–Fe basal-plane distance [11], which occurs despite a minor expansion along c [18]. The donation of the minority-spin electron from Fe^{2+} leads to an interaction that is weaker than, but not entirely unlike, the weak bonding of a transition-metal central-atom donor to a ligand acceptor where the donor orbital removes much of the ligand-field repulsion upon morphing into a weak bond. As observed in Ref. [30] on such an Au donor, ^{197}Au Mössbauer spectra also here still reflect the weakly-bonding donated pair, even though that particular Au orbital no longer affects the coordination geometry.

6. Conclusions

1. The lower homogeneity limit of $YBaFe_2O_{5+w}$ at 1000 °C is $w = 0.015(3)$ in equilibrium with O_2 of partial pressure $4.6{\cdot}10^{-16}$ bar that still maintains the phase while a lower value of $2.5{\cdot}10^{-16}$ bar causes reduction to metallic Fe. Equilibrium annealing of $YBaFe_2O_{5+w}$ with Fe at 450 °C yields $w = 0.012$.

2. The total entropy of the valence-mixing transitions is 8.9 ± 0.4 $Jmol^{-1}K^{-1}$ for twelve measurements of six $YBaFe_2O_{5+w}$ compositions within the $w = 0.015(3)$ limit. Of that entropy, 93% is achieved upon heating through the main Verwey transition of hysteresis ~4 K due to the long-range cooperative order of doubly-occupied d_{xz} orbitals. The remaining 7% is obtained at T_p of no hysteresis.

3. Calculation of orbital occupancies from experimental hyperfine parameters for $RBaFe_2O_5$ perovskites is possible because all Mössbauer components occur in pairs of various valence-mixing/charge-ordering degree, and this couples their concentrations. The method may be applicable to similar mixed-valence phases or cases where good estimates can be made for the orbital field, which, besides electron densities, requires information on the phase of the wave function.

4. The favored minority-spin electron occupancies sort out the Mössbauer-component pairs across the valence-mixing process: In charge ordered Fe^{2+} the electron occupies d_{xz} orbitals, in the intermediate component $d_{x^2-y^2}$ dominates (alternatively d_{xy}, see Supporting Material), in the valence-mixed component d_{z^2} dominates. The component pairs coexist at both T_V and T_p.

5. The minority-spin electron occupancies in $d_{x^2-y^2}$, d_{z^2}, d_{xz} extracted from Mössbauer spectra of $YBaFe_2O_5$ are of similar magnitude as those obtained by DFT calculations in Ref. [16].

6. As illustrated in the Supporting Material, replacing $d_{x^2-y^2}$ with d_{xy} yields qualitatively the same results, as only three of five d-orbital occupancies are generally independent upon least-squares fit of the $YBaFe_2O_5$ spectra.

7. Valence mixing in $YBaFe_2O_5$ achieves occupancies of d_{z^2} that would not be stabilized by the (square-pyramidal) ligand field. This illustrates that the valence mixing occurs between Fe atoms of the square bases that face directly each other and experience a weak Fe–Fe attractive interaction proportional to the degree of this valence mixing.

8. In the intermediate state between T_V and T_p, the occupancy of $d_{x^2-y^2}$ orbitals (alternatively d_{xy}; Supporting Material) complies with a weak checkerboard charge order indicated in Ref. [29].

9. In the charge ordered state below T_V, hyperfine parameters confirm ordering of the doubly occupied d_{xz} orbitals at Fe^{2+}.

10. Sharing the minority-spin electron implies degeneracy of the orbitals able to produce angular momentum along the spin moment. Neglecting this contribution to the internal field yields negative orbital

populations when fitting the spectra in the valence-mixed or intermediate state.

11. Mössbauer spectra detect all Fe participating in the overall AFM order below T_N as charge separated or valence mixed to a various degree. Non-AFM iron is due to domain walls and antiphase boundaries.

Acknowledgments

This research did not receive any specific grant from funding agencies in the public, commercial, or not-for-profit sectors.

Appendix A. Supplementary data

Supplementary data associated with this article can be found in the online version at http://dx.doi.org/10.1016/j.jssc.2017.04.036.

References

[1] R. von Helmolt, J. Wecker, B. Holzapfel, L. Schultz, K. Samwer, Giant negative magnetoresistance in perovskitelike $La_{2/3}Ba_{1/3}MnO_x$ ferromagnetic films, Phys. Rev. Lett. 71 (1993) 2331–2333. ⟨http://dx.doi.org/10.1103/PhysRevLett.71.2331⟩.

[2] S. Jin, T.H. Tiefel, M. McCormack, R.A. Fastnacht, R. Ramesh, L.H. Chen, Thousandfold change in resistivity in magnetoresistive La-Ca-Mn-O Films, Science 264 (1994) 413–415. ⟨http://dx.doi.org/10.1126/science.264.5157.413⟩.

[3] M. Pénicaud, B. Siberchicot, C.B. Sommers, J. Kübler, Calculated electronic band structure and magnetic moments of ferrites, J. Magn. Magn. Mater. 103 (1992) 212–220. ⟨http://dx.doi.org/10.1016/0304-8853(92)90255-M⟩.

[4] S. van Dijken, X. Fain, S.M. Watts, K. Nakajima, J.M.D. Coey, Magnetoresistance of Fe_3O_4/Au/Fe_3O_4 and Fe_3O_4/Au/Fe spin-valve structures, J. Magn. Magn. Mater. 280 (2004) 322–326. ⟨http://dx.doi.org/10.1016/j.jmmm.2004.03.030⟩.

[5] J.-B. Moussy, From epitaxial growth of ferrite thin films to spin-polarized tunnelling, J. Phys. D: Appl. Phys. 46 (2013). ⟨http://dx.doi.org/10.1088/0022-3727/46/14/143001⟩ (143001/1-27).

[6] J. Blasco, J. García, G. Subías, Structural transformation in magnetite below the Verwey transition, Phys. Rev. B 83 (2011). ⟨http://dx.doi.org/10.1103/PhysRevB.83.104105⟩ (104105/1-7).

[7] M.S. Senn, J.P. Wright, J.P. Attfield, Charge order and three-site distortions in the Verwey structure of magnetite, Nature 481 (2012) 173–176. ⟨http://dx.doi.org/10.1038/nature10704⟩.

[8] E.J.W. Verwey, Electronic conduction of magnetite (Fe_3O_4) and its transition point at low temperatures, Nature (London) 144, 1939, 327–328. ⟨http://dx.doi.org/doi:10.1038/144327b0⟩.

[9] F. Waltz, The Verwey transition - a topical review, J. Phys.:Condens. Matter 14 (2002) R285–R340. ⟨http://dx.doi.org/10.1088/0953-8984/14/12/203⟩.

[10] T. Kasama, R.J. Harrison, N.S. Church, M. Nagao, J.M. Feinberg, R.E. Dunin-Borkowski, Ferrimagnetic/ferroelastic domain interactions in magnetite below the Verwey transition. Part I: electron holography and Lorentz microscopy, Phase Transit. 86 (2013) 67–87. ⟨http://dx.doi.org/10.1080/01411594.2012.695373⟩.

[11] P.M. Woodward, P. Karen, Mixed valence in $YBaFe_2O_5$, Inorg. Chem. 42 (2003) 1121–1129. ⟨http://dx.doi.org/10.1021/ic026022z⟩.

[12] P. Karen, P.M. Woodward, Synthesis and structural investigations of the double perovskites $REBaFe_2O_{5+w}$ (RE=Nd, Sm), J. Mater. Chem. 9 (1999) 789–797. ⟨http://dx.doi.org/10.1039/A809302D⟩.

[13] P. Karen, P.M. Woodward, J. Lindén, T. Vogt, A. Studer, P. Fisher, Verwey transition in mixed-valence $TbBaFe_2O_5$: Two attempts to order charges, Phys. Rev. B 64 (2001). ⟨http://dx.doi.org/10.1103/PhysRevB.64.214405⟩ (214405/1-14).

[14] E.O. Wollan, W.C. Koehler, Neutron diffraction study of the magnetic properties of the series of perovskite-type compounds $La_{1-x}Ca_xMnO_3$, Phys. Rev. 100, 1955, pp. 545–563. ⟨https://doi.org/10.1103/PhysRev.100.545⟩.

[15] X. Hao, Y. Xu, M. Lv, D. Zhou, Z. Wu, J. Meng, Charge, orbital, and magnetic ordering in $YBaFe_2O_5$ from first-principles calculations, Inorg. Chem. 47, 2008, pp. 4734–4739. ⟨https://doi.org/10.1021/ic800060c⟩.

[16] C. Spiel, P. Blaha, K. Schwarz, Density functional calculations on the charge-ordered and valence-mixed modification of $YBaFe_2O_5$, Phys. Rev. B 79 (2009). ⟨http://dx.doi.org/10.1103/PhysRevB.79.115123⟩ (115123/1-13).

[17] P. Karen, Chemistry and thermodynamics of the twin charge-ordering transitions in $RBaFe_2O_{5+w}$ series, J. Solid State Chem. 177 (2004) 281–292. ⟨http://dx.doi.org/10.1016/j.jssc.2003.08.011⟩.

[18] P.M. Woodward, E. Suard, P. Karen, Structural tuning of charge, orbital, and spin ordering in double-cell perovskite series between $NdBaFe_2O_5$ and $HoBaFe_2O_5$, J. Am. Chem. Soc. 125 (2003) 8889–8899. ⟨http://dx.doi.org/10.1021/ja034813⟩.

[19] J. Lindén, P. Karen, $NdBaFe_2O_{5+w}$ and steric effect of Nd on valence mixing and ordering of Fe, J. Solid State Chem. 183 (2010) 2703–2713. ⟨http://dx.doi.org/10.1016/j.jssc.2010.09.012⟩.

[20] J. Lindén, P. Karen, Modeling hyperfine parameters observed from the charge-ordered to valence-mixed state of $NdBaFe_2O_5$, J. Phys.:Condens. Matter 24 (2012). ⟨http://dx.doi.org/10.1088/0953-8984/24/37/376002⟩ (376002/1-9).

[21] J. Lindén, F. Lindroos, P. Karen, Iron orbital occupancies upon valence mixing of charge-ordered $GdBaFe^{II}Fe^{III}O_5$, Hyperfine Interact. 226 (2014) 329–339. ⟨http://dx.doi.org/10.1007/s10751-013-0973-8⟩.

[22] P. Karen, Nonstoichiometry in oxides and its control, J. Solid State Chem. 179 (2006) 3167–3183. ⟨http://dx.doi.org/10.1016/j.jssc.2006.06.012⟩.

[23] A.C. Larson, R.B. Von Dreele, General Structure Analysis System (GSAS) Los Alamos National Laboratory Report LAUR 86-748, 2000.

[24] P. Karen, K. Gustafsson, J. Lindén, $EuBaFe_2O_5$: Extent of charge ordering by Mössbauer spectroscopy and high-intensity high-resolution powder diffraction, J. Solid State Chem. 180 (2007) 138–147. ⟨http://dx.doi.org/10.1016/j.jssc.2006.09.021⟩.

[25] J. Lindén, P. Karen, A. Kjekshus, J. Miettinen, T. Pietari and M. Karppinen, Valence-state mixing and separation in $SmBaFe_2O_{5+w}$, Phys. Rev. B 60, 1999, pp. 15251–15260. ⟨https://doi.org/10.1103/PhysRevB.60.15251⟩.

[26] J. Lindén, P. Karen, H. Yamauchi, M. Karppinen, Exploring the Verwey-type transition in $GdBaFe_2O_{5+w}$ using ^{57}Fe Mössbauer spectroscopy, Hyperfine Interact. 156–157 (2004) 321–325. ⟨http://dx.doi.org/10.1023/B:HYPE.0000043248.99004.65⟩.

[27] N.N. Greenwood, T.C. Gibb, in Mössbauer Spectroscopy, 1st ed. (Chapman and Hall, London 1971) pp. 66–67 and p. 11.

[28] J. Lindén, M. Karppinen, T. Shimada, Y. Yasukawa, H. Yamauchi, Observation of antiphase boundaries in Sr_2FeMoO_6, Phys. Rev. B 68 (2003). ⟨http://dx.doi.org/10.1103/PhysRevB.68.174415⟩ (174415/1-5).

[29] D.K. Pratt, S. Chang, W. Tian, A.A. Taskin, Y. Ando, J.L. Zarestky, A. Kreyssig, A.I. Goldman, R.J. McQueeney, Checkerboard to stripe charge ordering transition in $TbBaFe_2O_5$, Phys. Rev. B 87 (2013). ⟨http://dx.doi.org/10.1103/PhysRevB.87.045127⟩ (054127/1-5).

[30] M. Sircoglou, S. Bontemps, M. Mercy, N. Saffon, M. Takahashi, G. Bouhadir, L. Maron, D. Bourissou, Transition-metal complexes featuring Z-type ligands: Agreement or discrepancy between geometry and d^n configuration?, Angew. Chem. Int. Ed. 46 (2007) 8583–8586. ⟨http://dx.doi.org/10.1002/anie.200703518⟩.